JGR Solid Earth

RESEARCH ARTICLE
10.1029/2019JB017750

Dynamic Evolution of Permeability in Response to Chemo-Mechanical Compaction

Alice Macente[1,2], Tiziana Vanorio[1], Kevin J. Miller[1], Florian Fusseis[3], and Ian B. Butler[3]

[1]Department of Geophysics, Stanford University, Stanford, CA, USA, [2]Now at School of Geographical and Earth Sciences, Glasgow, UK, [3]School of Geosciences, Grant Institute, University of Edinburgh, Edinburgh, UK

Key Points:
- The presence of biotite prevents permeability along the loading direction and does not affect the permeability of the nearby layers
- In the absence of biotite, permeability is retained in pore connectivity
- Pressure-solution evolves accordingly to a texture-porosity coupling mechanism

Supporting Information:
- Supporting Information S1

Correspondence to:
A. Macente,
alice.macente@gmail.com

Citation:
Macente, A., Vanorio, T., Miller, K. J., Fusseis, F., & Butler, I. B. (2019). Dynamic Evolution of Permeability in Response to Chemo-Mechanical Compaction. *Journal of Geophysical Research: Solid Earth*, *124*, 11,204–11,217. https://doi.org/10.1029/2019JB017750

Received 28 MAR 2019
Accepted 5 NOV 2019
Accepted article online 11 NOV 2019
Published online 27 NOV 2019

Abstract Pressure-solution creep is an important fluid-mediated deformation mechanism, causing chemo-mechanical transformations and porosity and permeability changes in rocks. The presence of phyllosilicates, in particular, has previously been hypothesized to further reduce porosity and pore connectivity. Nevertheless, a full characterization of the spatiotemporal evolution of permeability during this process has yet to be reported. A pure NaCl aggregate and a mixture of NaCl and biotite were deformed through pressure-solution creep while monitoring their microstructural evolution through computed X-ray microtomography. The evolution of permeability and fluid velocity of the samples were computed by using the pore geometries from the X-ray microtomography as input for the Lattice-Boltzmann modeling. The results indicate that, as deformation proceeds, porosity and permeability decrease in both samples. In the salt-biotite sample pressure solution creep causes the formation of a compaction band perpendicular to the direction of loading, forming a barrier for permeability. Along the other two directions, pore connectivity and permeability are retained in the marginal salt layers, making the sample strongly anisotropic. The presence of biotite controls the way pore coordination number evolves and hence the connectivity of the pathways. Biotite flakes create an enhanced porosity decrease leading to compaction and reduction of pore connectivity. This reduction in porosity affects local stresses and local contact areas, reducing over time the driving force. According to a texture-porosity process, the reduction in porosity causes salt ions to dissolve in the marginal salt and precipitate within the biotite-bearing layer, where the bulk volume of salt grains increases over time.

1. Introduction

Fluid-rock interactions under stress have long been recognized as a contributing component of deformation mechanisms promoting porosity and permeability changes in the crust. Since both porosity (φ) and permeability (k) interplay in governing fluid mass content and transport rates through the pore network, they are both crucial time-variant properties controlling the deformation of rocks through fluid-mediated processes. This interplay is recognized to trigger chemo-mechanical transformations, such as mineral replacement reactions, alteration of primary porosity, and/or creation of secondary porosity (Jamtveit & Austrheim, 2010; Jolivet et al., 2005; Jonas et al., 2014) as well as modify rock elastic properties (Clark & Vanorio, 2016; Croize et al., 2010; Ehrenberg, 2006; Ghanbarzadeh et al., 2015; Urai et al., 1986; Vanorio, 2015; Zhang & Spiers, 2005). These interactions are also important during diagenesis and burial deformation, as they can produce new cement, either reducing porosity or creating new grain frameworks which resist to loading stresses, particularly in the case of mudrocks (Ilgen et al., 2017; Loucks et al., 2012). Where the porous medium compacts under stress, mass transport at the pore/grain scale influences the microstructural evolution of the porous system. Thus, studying the dynamic evolution of porosity and permeability during fluid-rock interactions helps understand how stress and reaction-transport in the subsurface affect rock microstructures and its properties (Yardley, 2011; Ghanbarzadeh et al., 2015; Gratier et al., 2013; Jamtveit & Austrheim, 2010; Kampman et al., 2014).

An important deformation mechanism resulting from fluid-rock interaction in stressed rocks is *pressure-solution creep (PSC)*. PSC is a solution mass transfer process responding to nonhydrostatic local stresses through which grains dissolve in more stressed areas, thus determining a stress-induced chemical potential gradient that triggers diffusion along the grain contacts (Fossen et al., 2007; Gibson, 1998; Gratier et al., 2013; Rutter, 1983). Diffusion then promotes transport of the solute through a fluid phase, allowing the

precipitation of the dissolved material in areas of lower stress (Gratier et al., 2013; Rutter, 1983). The slowest of these three important mechanisms (diffusion, transport, and precipitation) determines the rate-limiting process. Due to its occurrence in many lithologies and geological settings, PSC has been the focus of many studies (Aharonov & Katsman, 2009; Gratier et al., 2013; Renard et al., 2001; Renard et al., 2004; Rutter, 1983). In nature, PSC is often associated with deformation bands, representing low displacement deformation areas with enhanced cohesion and reduced permeability (Fossen et al., 2007; Sun et al., 2011) ultimately responsible for hydraulic compartmentalization of the rock (Ngwenya et al., 2003). Research studies have suggested that the presence of phyllosilicates affects PSC by modifying the rate of its fluid-enhanced deformation (Aharonov & Katsman, 2009; Hickman & Evans, 1995; Renard et al., 1997). Specifically, the presence of phyllosilicate minerals in deformational bands contributes to lowering the local permeability as compared to the host rock (Fossen et al., 2007; Heap et al., 2014; Renard et al., 2004).

Macente et al. (2018) studied the evolution of porosity and grain microstructures upon induced-PSC in samples imaged through X-ray computed microtomography (μCT) and analyzed using digital volume correlation. Two different sample compositions were tested: a pure NaCl sample (hereafter called "salt") and a mixture of NaCl and biotite grains (hereafter called "salt biotite"). The results of this work showed that the presence of biotite largely contributes to reduce porosity and increase local creep rates as compared to the pure NaCl layers. Nevertheless, direct observation of how PSC in the biotite-bearing layer reduces permeability over time and to what extent it controls its evolution remains to be assessed. Developing such an understanding is necessary because the behavior of reactive transport processes inherits dependencies related to the heterogeneous distribution of chemical agents in the subsurface, making the physical transport in the porous media heterogeneous.

In this study we test how PSC affects the dynamic evolution of permeability in the absence and presence of biotite, as well as the sensitivity of permeability evolution to the applied load direction. Permeability anisotropy in clays has been observed by Olsen (1960), Faulkner and Rutter (1998), Clennell et al. (1999), and Bayesteh and Mirghasemi (2015). Specific chemical processes responsible for enhancing PSC at pore- and grain-scale require close examination through dynamic imaging, which enables the direct monitoring of the ongoing processes and microstructure evolution. Two samples, a pure salt and a mixture of salt and biotite, were previously saturated with brine solution and left to compact for ~3 months to study the evolution of PSC and its effects on porosity and local strains (Macente et al., 2018). In this study, we performed Lattice-Boltzmann modeling (LBM) simulations on the acquired time-lapse μCT data sets of the sample volumes to calculate the effect of PSC on permeability. The sequential time series not only provides a visual characterization of the process and an assessment of the permeability evolution but also allows us to compute how pore-scale properties vary during the process. Assessing the dynamic change in pore-scale properties is key as it provides the opportunity to start linking the evolution of bulk permeability to pore attributes (i.e., local fluid velocity, pore coordination number, and surface area evolution) and how they are coupled or feedback upon each other. Changes in the local pore microstructure have been shown to be important factors in controlling changes in permeability (Bernabé et al., 2010; Clavaud et al., 2008; Doyen, 1988; Mok et al., 2002; Nelson, 1994; Noiriel et al., 2005).

2. Materials and Methods

The starting points for this study are the samples from the study by Macente et al. (2018), which used NaCl samples with two different compositions deformed by PSC. NaCl was chosen as rock-analogue geomaterial because previous compaction experiments have shown that it deforms quickly at room temperature and relatively low loads, thus making it an ideal candidate to study pressure-solution processes in the laboratory (Gratier, 1993; Renard et al., 2001; Renard et al., 2004; Schutjens & Spiers, 1999; Spiers et al., 1990). Den Brok et al. (1999) carried out similar experiments of PSC on $NaClO_3$, a type of salt that is known to not deform plastically at room temperature. Their findings showed that the behavior of $NaClO_3$ under PSC is strongly similar to the behavior of NaCl, proving that NaCl is also a suitable rock-analogue material to study PSC. In our experiment, both samples have initially the same diameter and height (5 mm by ~5 mm) as well as the same NaCl grain size (250–300 μm). Nevertheless, while the first sample consisted of pure NaCl grains, the second sample consisted of a mixture of NaCl grains and biotite flakes (4:1 ratio). Biotite was chosen because of its higher density and a higher attenuation coefficient than salt grains in the μCT and an easier

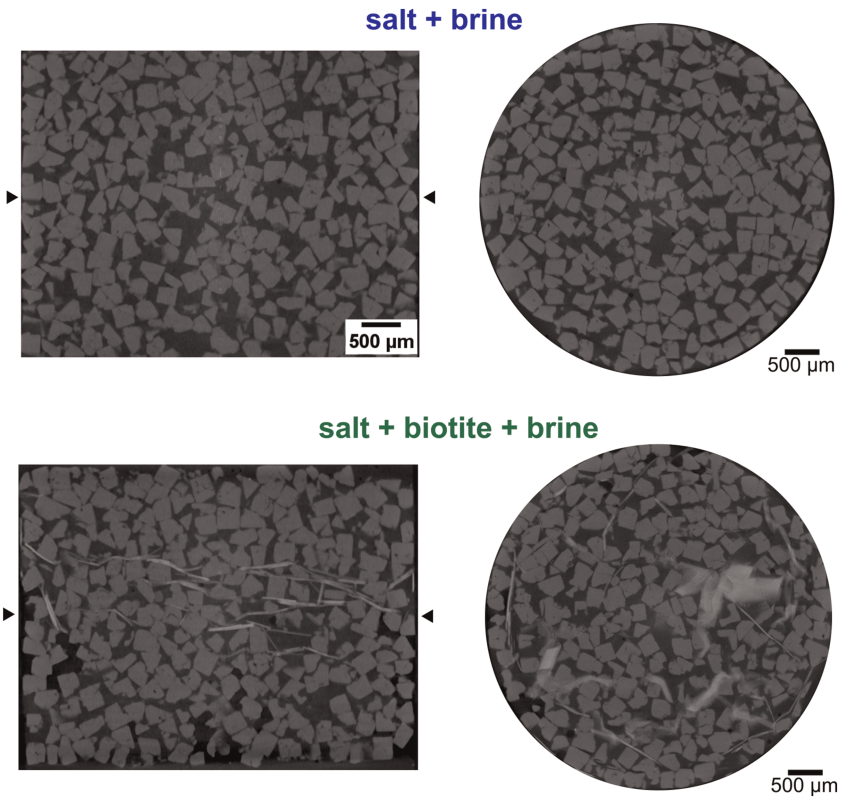

Figure 1. µCT slices of the zero time references along the *XZ* plane (vertical slice, left) and horizontal *XY* plane (right). The position of the *XY* plane along the *Z* axis is indicated by the black triangles on the side of the *XZ* plane image. Light gray indicates NaCl grains, the brightest features represent biotite flakes, and dark gray indicates brine-filled pores.

identification of the clay grains during compaction (Figure 1). The salt and biotite mixture was confined by two pure NaCl layers, acting as "reference" material within the sample to compare the degree of compaction under the same experimental conditions. Samples were initially loaded in in-house built X-ray transparent presses (Figure S1 in the supporting information) for 10 min by exerting a constant uniaxial load through a pneumatic actuator of 6.64 MPa. In this way, a precompacted starting material was created, which was CT-scanned and used as time zero reference (Figure 1). Subsequently, the experimental samples were flushed with saturated NaCl solution to ensure that the samples were fully saturated with brine and that no air bubble remained in the system. The solution was prepared in the laboratory by dissolving NaCl into deionized water until the solution became saturated (i.e., some NaCl was visible at the bottom of the fluid reservoir). The solution used as fluid reservoir was placed ~40 cm above the cells and connected to the lower fluid inlet of the cell (supporting information Figure S1). During scanning, samples were removed from the load: choke valves were used as shut-off valves for the air flow, enabling the air cable to be disconnected and the pneumatic actuator to unload the sample. Fluid connections were also closed, to ensure that the samples remain saturated. After imaging, each experiment was then reloaded to 6.5 (±0.1) MPa and left to deform for 2,455 hr (~3 months) along the vertical direction (*Z* direction). Compaction of the samples was monitored and bulk volume as well as porosity were calculated through 12 time-lapse µCT scans acquired in intervals over the duration of the experiment. During these extended loadings, the upper fluid connection was closed while the lower one was left open to ensure that samples remain saturated. The chemistry of the fluid reservoir was not monitored during the experiment.

To calculate permeability, we chose a time series consisting of seven µCT data sets capturing different stages of compaction. From these µCT data sets, we selected subvolumes of ~400^3 voxels (~17.6 mm^3) centered in the middle of the sample (Figure 2). The height of these subvolumes changed upon compaction, with the volume reducing to 400 * 400 * 360 voxels at the end of the experiment. LBM was conducted on the segmented pore space of the subvolumes by using a single-phase LBM approach as described in Keehm (2003) and

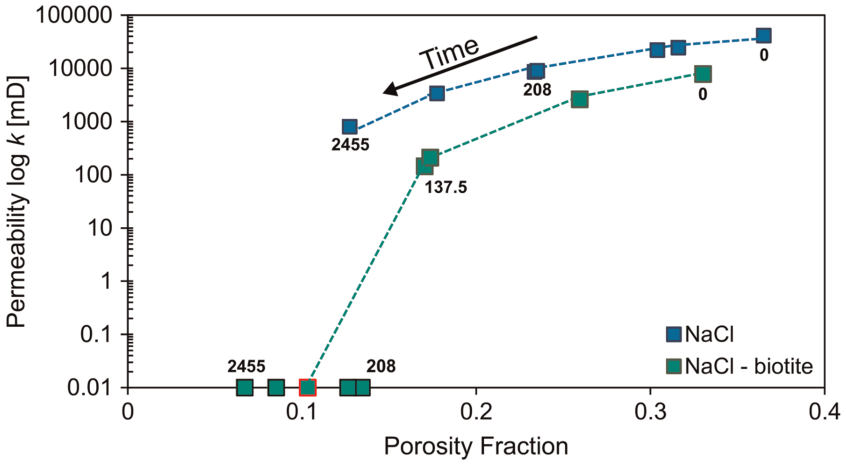

Figure 2. Porosity-permeability (in log scale) plot for the NaCl (blue) and NaCl-biotite sample (green) showing the evolution of permeability over time along the loading direction. Labels in bold next to data points indicate the time of compaction in hours. The red square represents the average porosity fraction of four different volumes at different compaction times, exhibiting no flow.

Miller et al. (2017). In Macente et al. (2018), results pointed to the fact that the positive feedback created by the pressure-solution mechanism arises on scale lengths much larger than the grain diameter. Above centimeter-scale lengths, advection is required to transport dissolved phases in solution to new precipitation sites (Gratier et al., 2013). The rate limiting step for PSC in NaCl is diffusion-controlled (Spiers & Brzesowsky, 1993). These facts would imply the use of a chemo-hydro-mechanical model approach. However, previous studies have shown that LBM can handle complicated pore geometries as well as detect small pore structure variations (Keehm et al., 2001). LBM uses laminar flow to solve the Navier-Stokes equation and it therefore uses a simplified approach to model permeability of deformed salt samples via PSC as compared to chemo-hydro-mechanical modeling.

Segmentation of the pore space was obtained using the interactive threshold operator in Avizo®, to produce binarized images. The sensitivity of the segmentation to changes in the threshold values was established by repeating the procedure on volumes that were eroded and dilated by one voxel (see Fusseis et al., 2012, and Macente et al., 2017, 2018). LBM treats the volume of fluid as a collection of particles whose flow is represented by a particle velocity distribution function at each grid point. The velocity is obtained by calculation of the hydrodynamic moments of that function. A pressure boundary condition, acting as driving force for fluid flow, is imposed along one of the three spatial directions (X, Y, and Z) using a density perturbation function. A no-flow boundary condition is applied at the sidewalls of the sample, perpendicular to the pressure gradient. The fluid velocity vector field for the laminar flow is obtained once the finite solution converges (Miller et al., 2017; i.e., permeability did not change more than 0.0001% for 40 iterations) and the permeability stabilized to a steady state. The fluid velocity fields are rendered in 3-D in lattice units; that is, the physical system is first converted into a dimensionless one, independent of both the original physical scales and simulation parameters. Such a dimensionless system is then converted into a discrete simulation. Permeability is then calculated along the direction of the flow using Darcy's law, by volume-averaging the local fluid velocity (Keehm, 2003). The calculation of permeability is repeated in all three directions of the samples, by changing the direction of the imposed flow.

Furthermore, we extracted three layers from the salt-biotite sample: a central biotite-bearing layer and two marginal salt layers (see supporting information Figure S2). We then calculated the permeability of each of these layers in all directions, so as to investigate to what spatial extent the presence of biotite affects the permeability of the adjacent layers. We also calculated the bulk volume of salt in the central biotite-bearing layer for increasing deformation, by (1) identifying the subvolume containing the biotite-bearing layer, (2) segmenting the salt grains present in it through interactive thresholding, and (3) applying the volume fraction operator to calculate the bulk volume percentage of the segmented salt. Error bars of ±5% have been estimated by taking into account miscalculation of the cross-sectional slices defining the top and bottom

boundaries of the biotite-bearing layer for each time interval considered and by recalculating the new bulk volume occupied by the salt grains.

We also sought the relationships between permeability and porosity, on one hand, as well as the coordination number between the pores and the main flow stream and pore surface area, on the other, to explore the functional relationships between changes in bulk properties upon PSC and the associated pore-system attributes. For this purpose, the segmented pore geometry, derived from Macente et al. (2018), was skeletonized using a medial-axis thinning algorithm (see supporting information and Figure S2). For each pore, the coordination number (from 1 to 8) was calculated by identifying how many edges are connected to one node. A coordination number of one means that a pore is connected to the main flow stream by one pore throat only; thus, they are called dead-end pores. Dead-end pores can therefore be seen as stagnant fluid pockets. Finally, we tracked the dynamic evolution of the pores surface area as the sample undergoes deformation (see supporting information).

3. Results

The compaction experiments provide two microstructures exhibiting a different evolution of permeability along the *Z* direction (Figure 2). At first, both samples exhibit a similar decrease in permeability, even though their starting porosity is slightly different (~36% and ~33%). Over time, however, the two trends diverge. While the salt sample shows a steady decrease in permeability (k), the salt-biotite sample exhibits a tipping point as it reaches a porosity of ~17% after 137.5 hr of compaction, marking a sharp decrease in permeability (Figure 2). Beyond this point, the permeability of the salt and biotite sample drops to 0 (Figure 2).

These permeability trends are accompanied by a different evolution of the sample microstructures. The gradual compaction of the pure salt sample provides microstructures that are characterized by a decrease in porosity being homogeneously distributed throughout the sample (Figures 3a and 3b), yet the salt grains seem to mostly retain the cubic shape as evidenced by the presence of sharp edges and corners (Figure 3c). Only a few areas of the sample exhibit some degree of indentation (Figures 3c). Conversely, in the salt-biotite sample the reduction in porosity reveals a heterogeneous distribution, being more pronounced within the biotite-bearing layer near the biotite flakes (Figures 4a and 4b). Within this layer, grains appear to have lost their cubic shape due to a much greater degree of indentation, eventually leading the grains to fuse together (Figure 4c).

The different evolution of the microstructure also controls the distribution and evolution of the fluid velocity pathways modeled within the sample volume (Figure 5). In the precompacted stage of the pure salt sample, the velocity streamlines are equally distributed throughout the entire volume, likely due to a large homogeneous pore network (Figure 5a). As compaction proceeds, both the number of the connected fluid conduits and the magnitude of fluid velocity are reduced, leading the flow paths to organize primarily as uniform dispersed channels. Overall, this rearrangement of the microstructure leads to fewer and narrower pore throats displaying higher velocity magnitudes (Figures 5b and 5c). Conversely, the velocity pathways within the salt-biotite sample evolve through a different sequence of microstructures. Initially, higher fluid velocities are localized in the middle of the sample, within the biotite layer, where the flakes of biotite partially occlude the intergranular porosity, likely reducing the pore throats and hence locally enhancing fluid velocity (Figure 5a′). As compaction proceeds, however, the sample experiences a sharp disruption in its connected porosity, which occurs at earlier compaction stages than the pure salt sample. Such a connectivity breach drastically reduces the number of fluid channels leading the velocity magnitude of the fluid streams to cease (Figure 5b′). As a result, the fluid velocity field within the last measurable permeable microstructure appears to be highly dominated by very localized and tortuous channels, still exhibiting higher velocity across the biotite-bearing layer (Figure 5b′). Such evolution of the pore system translates into a salt-biotite microstructure that is highly anisotropic with regard to the permeability (Figures 6a and 6b). It is worth pointing out that the presence of the biotite-bearing layer seems neither to affect the compaction of the adjacent salt layers sitting above and below it nor the permeability. In fact, when digitally separating the salt-biotite sample into three layers (i.e., the central biotite-bearing layer and two marginal salt layers), the permeability of the marginal salt layers (green diamonds in Figure 6 c) mimics exactly the evolving permeability of the pure salt sample. This observation is also supported

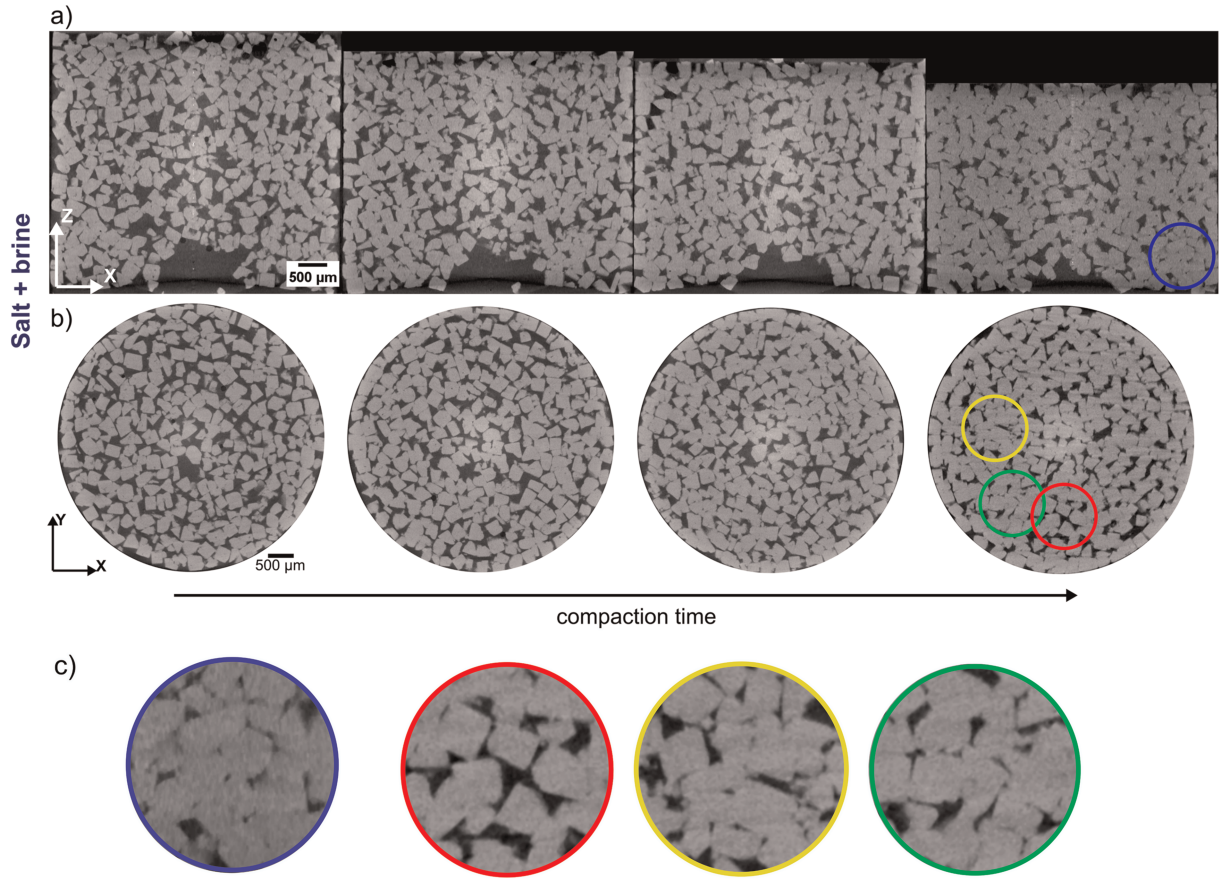

Figure 3. µCT slices showing the evolution of the microstructure for the pure salt sample: (a) Vertical XZ µCT slices, cut from the middle of the sample; (b) *XY* slices, half height of the sample; (c) zoom-in of the areas in (a, b) highlighted by the circles showing grains retaining pseudo-cubic habits (in red) and regions of greater porosity reduction and indented grains leading to fusion (blue, yellow, and green).

by the preservation of the velocity fluid streams within the marginal salt layers along the *X* and *Y* directions (supporting information Figure S4).

To understand the extent to which the biotite flakes affect the pressure-solution of salt grains, we calculated the bulk volume occupied by the salt grains within the three different layers, reported as volume of salt in Figure 7. The volume of salt in the marginal salt layers is reported as average between these layers. Although the precompaction stage shows similar volumes characterizing the three layers, the volume of salt exhibits a different evolution. As the sample progressively compacts, we found that the bulk volume occupied by the salt grains in the biotite-bearing layer generally increases over time, while the change in the marginal salt layers is not clearly perceptible (Figure 7).

To understand the role of how pore scale parameters contribute to regulating the different evolution of the microstructure of the two samples and its macroscopic permeability, we investigated how the relationship between permeability and pore coordination number (Figure 8) and pore surface area (Figures 9) evolves over time. Figure 8 reports the evolution of coordination numbers equal to one (C = 1, "dead-end pores") and three (C = 3). We focus on these specific coordination numbers because their evolution over time contributes to more than 90% of the change in pore connectivity. In the graphs of Figure 8, the frequency of each coordination number was normalized to the sum of the coordination number contributions computed in each sample volumes (i.e., salt and salt biotite). Initially, both samples show similar frequency; over time, however, the frequency of these coordination numbers evolves markedly differently (Figures 8a and 8b). In particular, the single biotite layer shows the frequency of pores being characterized by coordination number equal to one (C = 1, dead-end pores) to increase up to ~73%; instead, pores with coordination number equal to three (C = 3) decrease up to ~24%. Moreover, both samples exhibit similar trends but different

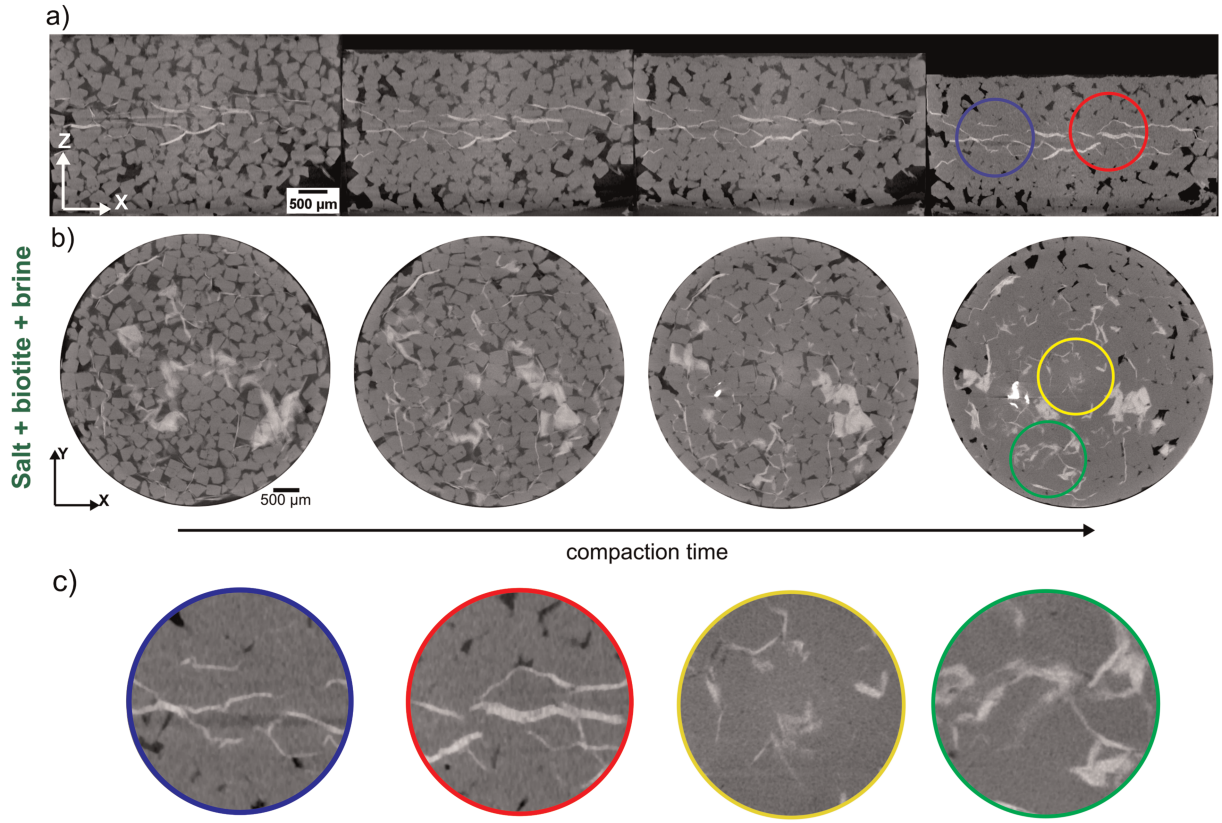

Figure 4. μCT slices showing the evolution of the microstructure of the salt-biotite sample: (a) Vertical *XZ* μCT slices, cut from the middle of the sample; (b) *XY* slices from half height of the sample; (c) zoom-in areas of regions in (a) and (b) highlighted by circles that show indented grains fusing together leading to a greater reduction in porosity.

magnitude of changes, with the salt-biotite sample presenting a variation in frequency that is five times larger than the pure salt sample (Figures 8a and 8b). The marked increase in C = 1 pores within the salt-biotite sample occurs between 137.5 and 208 hr of compaction (red arrows in Figure 8), corresponding to the time interval before which permeability drops to 0. Furthermore, it is worth noting that the evolution of the coordination number of the pores characterizing the salt-biotite sample lies between the evolution of the pure salt sample and the biotite-bearing layer, likely arising from the inherent composite nature of the biotite and salt grains mixture. Figures 8a and 8b also show that trends of the coordination numbers for this sample are closer to those characterizing the pure-salt sample, given that the salt volume layers constitute two thirds of the whole salt-biotite sample.

We also analyzed the evolution of the total pore surface area as a function of time, which is shown in Figure 9. As with the other parameters being considered, the two sample compositions start with similar values of pore surface area. However, the pore surface area within the salt-biotite sample displays a rate of reduction that is more pronounced compared to the pure salt sample. Over the whole deformation range, the total pore surface area in the salt-biotite sample decreases by ~70% while it reduces by ~50% in the pure salt sample (Figure 9). The two samples seem to display different rates of change immediately after the first hours of compaction, with the salt-biotite exhibiting a higher rate then settling on a more similar evolution after the breakdown in pore connectivity showed by the model.

4. Discussions

Continuum-scale reactive-transport models rely on an accurate choice of pore-scale parameters at the micro-scale and/or nanoscale so as to effectively describe the control on and the relationships with properties measured at macroscale (e.g., chemical rate kinetics, porosity, and permeability). The lack of physical

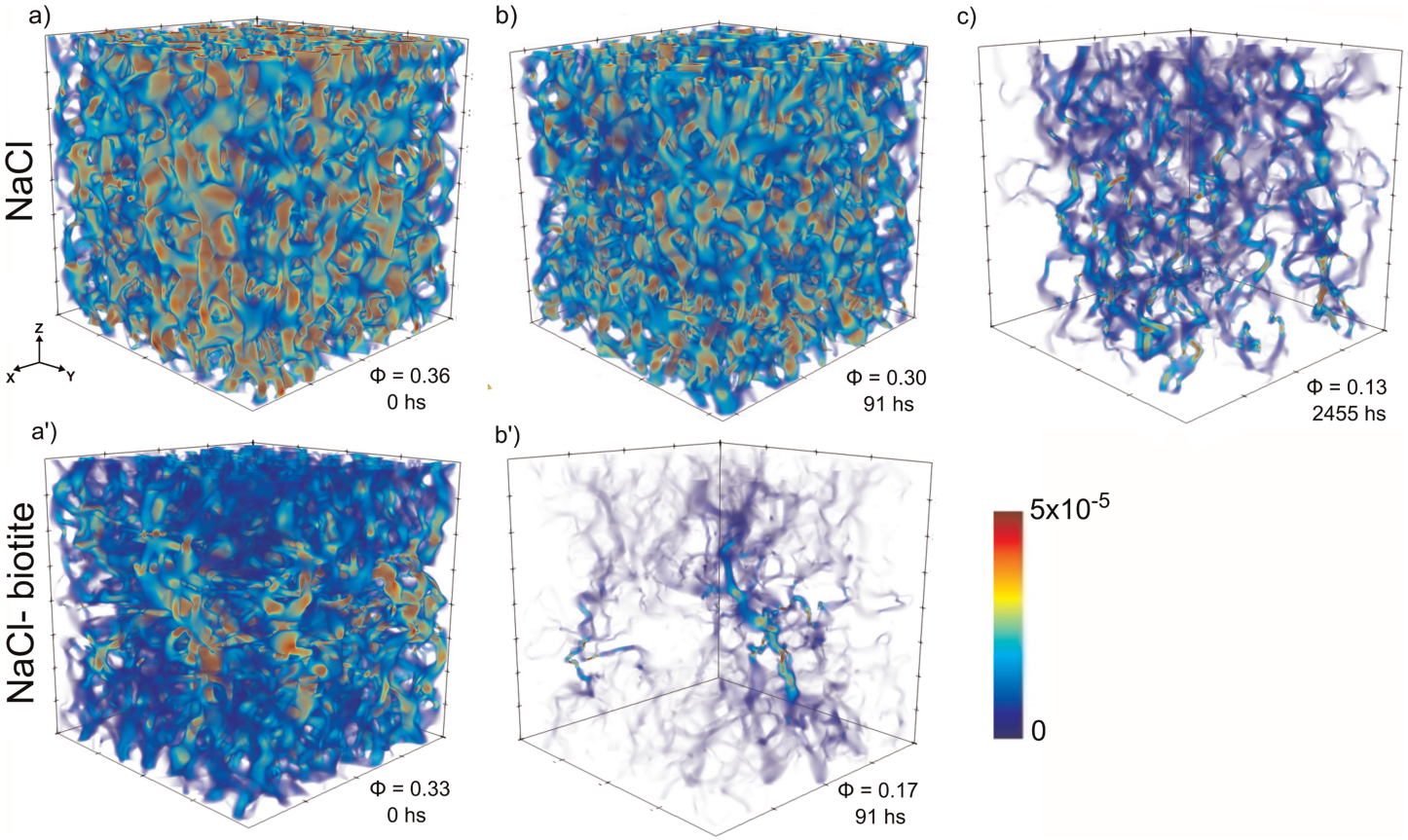

Figure 5. Three-dimensional renderings of the evolution of the fluid velocity field within the pure salt sample (a–c) and the salt-biotite sample (a′–b′), both along the *Z* direction. The salt-biotite data set is not displayed at 2,455 hr of compaction because flow ceases after 91 hr of compaction. Each sample volume is labeled with the porosity fraction (φ) attained at different times (in hours, "hs") of the compaction stages. In the figure, warmer colors indicate high magnitudes of fluid velocity being reported in lattice units. As compaction proceeds, the number of fluid channels is reduced as well as their velocity magnitude, localizing flow along few dispersed and tortuous channels (salt sample, a–c); in the biotite-bearing sample the rate of such a reduction is faster, with very few fluid channels active at 91 hr, then velocity ceases entirely. Side length is 2.6 mm.

understanding of the evolution of pore-scale parameters and their calibration limits our ability of applying continuum models to chemical fluid-rock interactions. To start formulating conceptual models that capture 4-D changes in storage and transport properties, there is the need for studying (a) dynamic changes in rock porosity and permeability upon fluid-rock interactions, (b) the effect that physical and chemical heterogeneities produce over small length scales, and (c) feedback between pore-scale parameters and porosity-permeability in the presence of these small length-scale heterogeneities. In this study, the combination of dynamic CT imaging with LBM enabled the quantification of pore-scale changes during PSC and their effect on macroscale properties in the presence and absence of phyllosilicates. When computing LBM, we treated the compaction of the samples as inducing interstitial fluid movement, being squeezed through the pore space and creating localized fluid pressure gradients. Hence, the evolution of the pore-scale attributes, obtained by computing LBM, critically affects the distribution and evolution of the local pressure gradients. In turn, these affect local fluid velocity and the distribution and transport of solutes. This modeling allows us to track how the macroscale properties permeability evolves on the basis of pore-scale attributes and local heterogeneities (i.e., biotite) during PSC.

4.1. Interpretations From LBM Analyses

The LBM approach we used is a single phase model (Miller et al., 2017). It has been shown that single-phase LBM methods successfully calculate permeability in porous media with less computational power, without sacrificing the underlying physics (Xing et al., 2007).

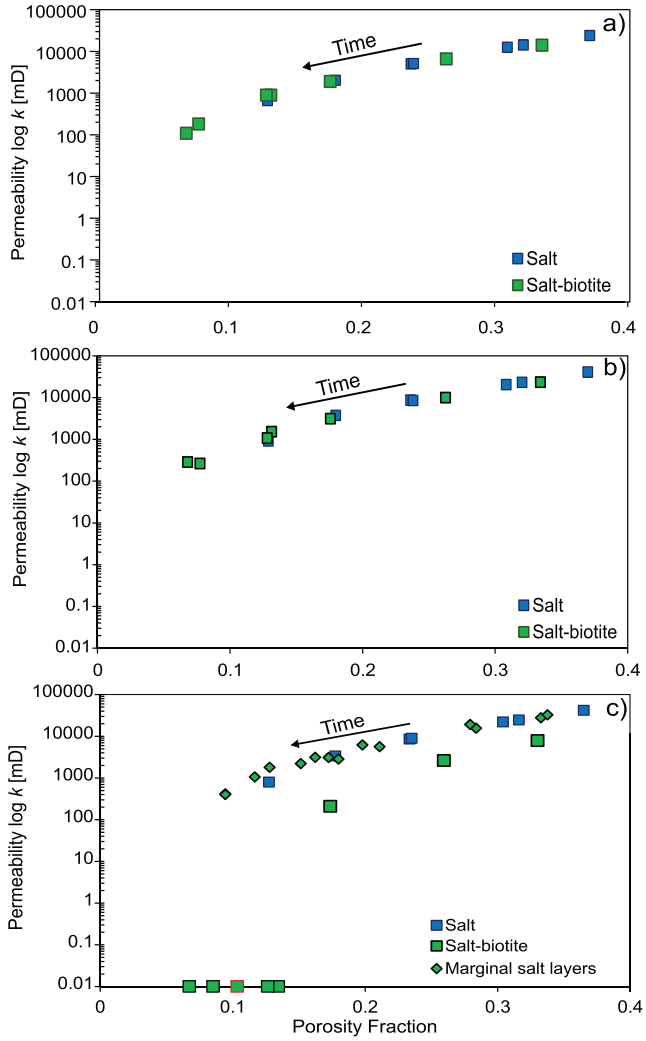

Figure 6. Porosity-permeability (log(k)-Φ) plot computed along the *Y* (a) and *X* directions (b) of the salt and the salt-biotite samples. The two samples do not show any difference in the permeability trends. (c) Porosity-permeability trend computed within the marginal salt layers in the salt-biotite sample (green triangles), *Z* direction. The permeability of the marginal salt layers follows the same trend exhibited by the pure salt sample (blue squares), indicating that their compaction is not affected by the presence of biotite in the central layer within the experiment timeframe.

The initial permeability values of our samples approximate those describing unconsolidated coarse sand grains of similar size (Beard & Weyl, 1973; Nelson, 1994). The permeability of the pure salt sample gradually decreases over time while remaining isotropic, in agreement with the findings by Renard et al. (2004). In contrast, the salt-biotite sample shows a steady reduction in permeability along the loading direction (*Z* axis) before exhibiting a sharp change. At first, permeability varies across 2 orders of magnitude reaching a tipping point at 137.5 hr of continuous compaction. After this point, permeability rapidly goes to 0 experiencing a change in porosity of ~4% (from ~17% to ~13%). Tipping points similar to those observed in this study were also reported by Van der Land et al. (2013) along permeability trends being computed in 3-D synthetic volumes generated from 2-D textural images of noncompacted carbonate sediments. The authors used the results from their permeability modeling to reconstruct the burial history of a carbonate formation and informed basin modeling to provide constraints on diagenetic scenarios. Our results provide an experimental foundation for a process that they introduced previously only theoretically. Also Bourbié and Zinszner (1985) showed a tipping point at porosity ~8–9% for Fountainebleau sandstones, at which the porosity/permeability power law changes exponent. The type of deformation mechanism has been shown to critically influence the porosity/permeability relationship and hence affects porosity threshold (Bernabé et al., 2003). Chemical processes, that is, pressure-solution, often produce roughness on the pore surfaces, which may form fractal structures. These, in turn, can be responsible for the creation of noneffective porosity and critically lower the permeability of the porous medium (Bernabé et al., 2003; Nelson, 1994; Pape & Schopper, 1988; Pape et al., 1999). The comparison between the two samples along with the analysis of pore-scale attributes and their evolution upon compaction enabled us to identify to what extent the presence of phyllosilicates affects the PSC process and the dynamic evolution of porosity-permeability. The analysis of the velocity streamlines along the *Z* direction showed that the pure salt sample is initially characterized by a homogeneous distribution of high velocity paths. Under the assumption that local velocity magnitude is a proxy for solvent flux, this indicates the absence of preferable and/or predetermined sites at which dissolution may occur (Figure 5a). After 2,455 hr of compaction, streamlines are reduced in number but those being characterized by high velocity are still present (Figure 5c). This indicates that the feedback between the change in porosity and local flow field is still ongoing and hence, changes in surface area (Figure 9) upon which the overall reaction rate depends (Yoon et al., 2015) and dissolution are also still ongoing. In contrast, in the salt-biotite sample the high velocities of the streamlines are initially localized within the biotite-bearing layer (Figure 5a′). We believe that the initial presence of pore throats within the biotite layer, responsible for lower porosity and high velocity of the fluid, represents a physical and a chemical heterogeneity, which translates into a chemical potential at the interface between salt and biotite grains, favoring dissolution and porosity reduction, and hence an initial localization of PSC (Figure 10b; Aharonov & Katsman, 2009; Greene et al., 2009). Factors such as particle shape, particle size, and the shape of the contact area may further contribute to the initial porosity reduction within the biotite-bearing layer and hence, to high fluid velocities (Meyer et al., 2006; Pluymakers & Spiers, 2015; van den Ende et al., 2018). Since reactive-transport distances during pressure solution of NaCl grains in a stagnant, saturated brine environment are assumed to be on the order of the grain size, the transported solute reprecipitates in the nearby pore space (e.g., Gratier et al., 2013; Gundersen et al., 2002; Weyl, 1959). This implies that, over the first 137.5 hr of compaction, PSC localizes within the biotite-bearing layer and material reprecipitates in the nearby pore space. Over time, the resulting reduction in porosity and pore

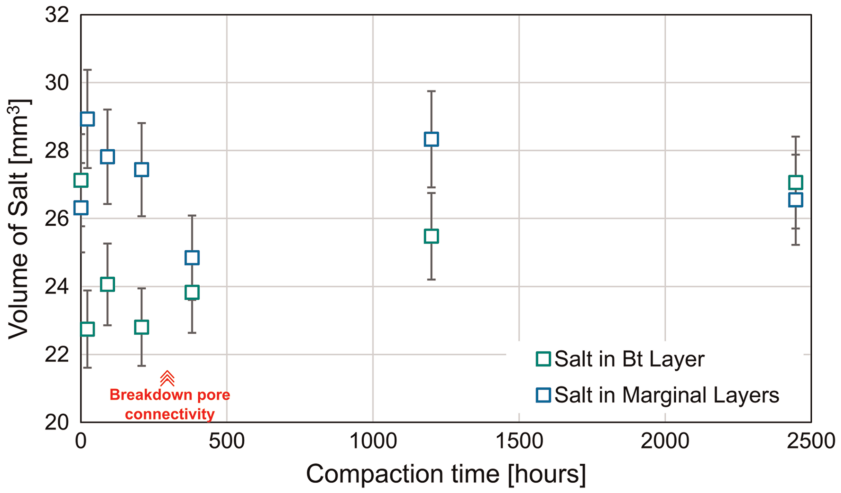

Figure 7. Evolution of the bulk volume of salt in the individual biotite-bearing layer ("Bt layer," green squares) and the marginal salt layers (average of the blue square values). As compaction proceeds, the volume of salt in the biotite-bearing layer increases, suggesting more salt being transported toward this layer and aggrading overtime. The plot also reports the time at which pore connectivity breaks down in the sample (red label).

connectivity in the biotite layer, as evidenced by the experimental data, is such to prevent permeability along the *Z* direction, at least at the resolution of our data (Figure 5).

4.2. Influence of Grain Packing and Clay Distribution

The initially different degree of grain packing may have played a role in controlling the different evolution of permeability in the two systems. Studies on natural samples (sandstones vs. carbonates) have shown that permeability increases with an increased degree of grain sorting (Krumbein & Monk, 1943; Hiatt & Kyser, 2000), while it decreases with increasing compaction and cementation, and hence burial depth. Similarly, different clay types may also affect the evolution of porosity/permeability relationship (Hiatt & Kyser, 2000). In our specific case study, the microstructural change we observed in the marginal salt layers is not the same as of the pure salt sample, indicating that the initial different grain packing is not solely responsible for the different microstructural evolution. Rather, we infer the microstructural evolution of the marginal salt layers, which display a much higher degree of salt grains fused together as compared to the pure salt

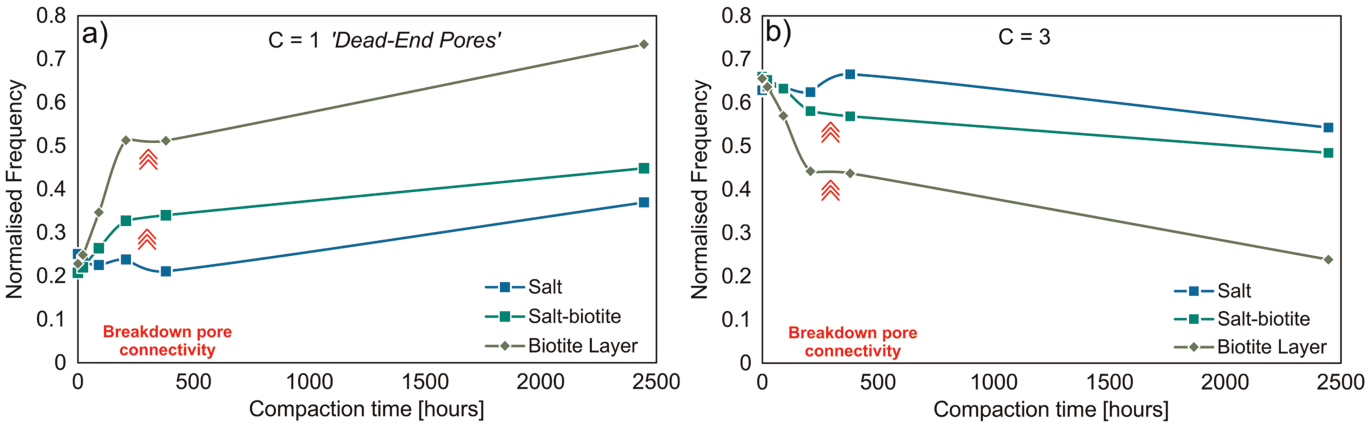

Figure 8. Normalized frequency of pore coordination numbers equal to one (C = 1, a) and three (C = 3, b) as a function of compaction time. Data refer to the pure salt sample (blue squares), salt-biotite sample (green squares), and biotite-bearing layer alone (dark green diamonds). Over the duration of compaction, coordination numbers equal to one and three increase and decrease, respectively. We normalized the frequency of each coordination number to the sum of the coordination number contributions to each data set. The frequency of dead-end pores dramatically increases over time in the central biotite layer. The time at which pore connectivity most likely breaks down before permeability drops to 0 in the salt-biotite sample is labeled in red and marked with red arrows.

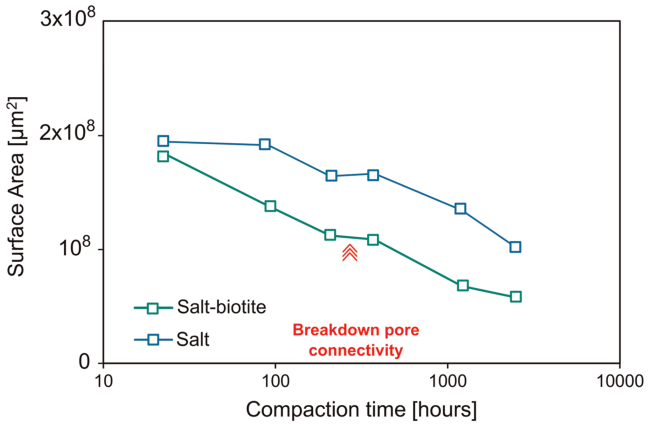

Figure 9. Pore surface area-(log) time evolution for the two sample compositions. The time at which pore connectivity most likely breaks down before permeability drops to 0 in the salt-biotite sample is labeled in red and marked with red arrows.

sample, to be affected by the presence of the nearby biotite-bearing layer, although they still retain a permeability evolution similar to the pure salt sample. The presence of biotite does not affect the evolution of permeability in the marginal salt layers, but it does influence the extent of the process and local porosity evolution. The biotite layer was prelocalized in the middle, because two reference materials, confining the layer, were needed. The biotite grains were not deliberately oriented in any way during loading. We argue that, despite having a prelocalized biotite layer in the middle of the sample, the biotite grains were not preferentially oriented and over time they localised furthermore the process in the central layer. In natural reservoirs, clays would be randomly distributed in the medium, future experiments will consider to have a fully random distribution in the system, to verify whether biotite grains preferentially localised and orient over time.

4.3. Evolution of PSC as a Texture-Porosity Coupling Process in the Presence of Biotite

Macente et al. (2018) indicated that the reduction in porosity within the biotite-bearing layer is not accommodated by pore collapse during compaction but rather by progressive precipitation of salt filling the pore space, which follows a texture-pressure coupling process (Dewers & Ortoleva, 1988; Merino et al., 1983; Ortoleva et al., 1987). According to the texture-pressure coupling model proposed by Merino (Merino et al., 1983), dissolved material diffuses from areas with higher porosity toward areas with relatively low porosity, which means from areas where grain contacts are characterized by smaller contact points and higher stresses to those where grains have larger grain contact areas and, correspondingly, lower stresses (Dewers & Ortoleva, 1988; Merino et al., 1983; Ortoleva et al., 1987). According to Merino's model, this means that in our data the dissolution front migrates from the more porous marginal salt layers whose grain contacts have smaller contact areas and hence higher stresses at contact points toward the biotite-bearing layer. We found that the breakdown in pore connectivity within the biotite-bearing layer corresponds to the largest number of dead-end pores and the continuous

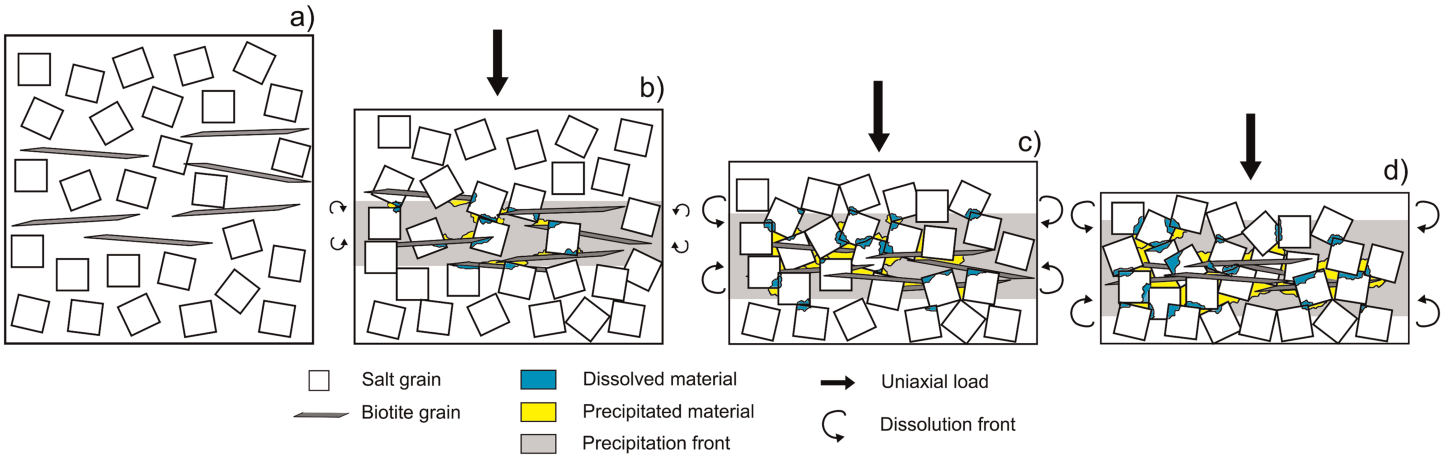

Figure 10. Sketch illustrating the enhancement of PSC in the presence of biotite. The black arrows indicate the active dissolution front, while the shaded gray areas represent the precipitation front. (a) Initial state. (b) Uniaxial load is applied and the grains start to arrange due to mechanical compaction. Higher porosity reduction is seen in the biotite-bearing layer favoring higher chemical potential gradient between dissimilar phases, the biotite flakes and the halite grains, and hence initial dissolution (Aharonov & Katsman, 2009; Greene et al., 2009). This causes contact areas to increase and stresses at local points to decrease. (c) The feedback dissolution-precipitation process that follows Merino's model (Merino et al., 1983): Dissolution starts in high porous areas, where grain contact areas are smaller and stresses are higher (cyan shaded areas) while precipitation occurs in the less porous areas, where grain contact areas are higher and stresses are smaller (yellow areas). This leads the salt to dissolve in the marginal salt layers and precipitate within the biotite-bearing layer, where the bulk volume of salt increases over time. (d) This positive feedback continues until the high number of dead-end pores in the biotite-salt layer prevents permeability in the localized biotite layer, leading to the formation of a compaction band perpendicular to the loading direction. The precipitation front migrates toward the marginal salt layers.

reduction in pore surface area (Figures 8 and 9). These changes cause, respectively, permeability and transport to cease as well as the contact areas in the biotite layer to increase (Figure 10b), thus reducing the driving force for the diffusion process to continue. Upon reaching this stage, fluid velocities cannot be calculated because of the high number of dead-end pores inhibiting permeability. As this flow barrier forms, salt precipitates and accumulates, causing the precipitation front to further migrate toward the marginal salt layers, according to Merino's hypothesis (Figure 10c), and as evidenced by the increase in salt volume within the biotite-bearing layer between 150 and 400 hr of compaction (Figure 7). The overall chemo-mechanical process forms a localized compaction band, which is perpendicular to the loading direction acting as a structural heterogeneity. Pore connectivity is thus retained only in the marginal salt layers, thus inducing permeability anisotropy (Figures 3a, 10d, supporting information Figure S4) (Olsen (1960); Faulkner & Rutter (1998); Clennell et al. (1999); Bayesteh & Mirghasemi (2015); Rotevatn et al. (2016)).

Looking at the process from a different perspective, we observe that the velocity fields measured along the directions perpendicular to the load (X, Y) show initially higher velocities in the marginal salt layers (supporting information Figure S4), indicating that pore connectivity is preserved and that potential turbulent flow at the pore scale may be present (Figure 10c). The results show that the loading direction strongly controls the evolution of microstructures affecting the macroscale properties.

5. Conclusions

As time goes by, it becomes apparent that chemo-mechanical processes in porous rocks require more understanding of the scale-dependent mechanisms (from nano-to-micro-to-macro) that fit together in increasingly complex dynamics. Dynamic (4-D) imaging from computed X-ray microtomography coupled with LBM is used as a powerful tool to visualize processes in porous media (from natural fluid-mediated diagenesis to human-induced injections) as well as capture properties and geometries across scales, allowing us to study how macroscale properties depend on the evolution of pore-scale parameters. We report the first dynamic evolution of permeability upon PSC in the presence and absence of biotite and quantify its dependence on pore-scale properties. The relationships between bulk scale properties, namely, permeability and porosity, and pore-scale parameters, namely, pore coordination number and surface area, show how microscale-macroscale parameters critically feedback upon each other, having important implications for fluid migration. The presence of a biotite-rich layer localizes the PSC process due to the lower local porosity, favoring a chemical potential gradient at the interfaces between salt and biotite grains and hence, diffusion. We comprehensively looked at our results within the framework of the texture-porosity model proposed by Merino (Merino et al., 1983). In light of this model and the results from this study, we postulate that diffusion goes from the marginal salt layers, where the grain contact areas are smaller, toward the biotite-bearing layer, where the grain contact areas are larger due to the lower porosity. Because of this ion migration, salt being dissolved in the marginal salt layers deposits over time toward the biotite-bearing layer, whose bulk volume of salt grains therefore increases over time. This causes the sample to become strongly anisotropic. Permeability anisotropy has been observed in consolidated and unconsolidated sedimentary and reservoir rocks and critically constitutes an important parameter to take into consideration for reservoir modeling. Overall, this study provides new insights on parameters informing pore-scale modeling during enhanced chemo-mechanical compaction. Furthermore, time-lapse measurements on 3-D printed microstructure that evolve with time (Head & Vanorio, 2016) can be seen as a natural extension of the dual-scale approach reported in this study so as to extend the scale of observation to physical measurement on tangible microstructures.

Acknowledgments
This work was supported by the NSF CAREER Award (EAR-1451345 to T. V.). The data presented in this manuscript are provided through Figshare (https://figshare.com/projects/Dynamic_Evolution_of_Permeability_in_Response_to_Chemo-Mechanical_Compaction/67736). LBM was performed through Matlab®.

References

Aharonov, E., & Katsman, R. (2009). Interaction between pressure solution and clays in stylolite development: Insights from modeling. *American Journal of Science*, *309*, 607–632. https://doi.org/10.2475/07.2009.04

Bayesteh, H., & Mirghasemi, A. A. (2015). Numerical simulation of porosity and tortuosity effect on the permeability in clay: Microstructural approach. *Soils and Foundations*, *55*, 1158–1170. https://doi.org/10.1016/j.sandf.2015.09.016

Beard, D. C., & Weyl, P. K. (1973). Influence of texture on porosity of unconsolidated sands. *American Association of Petroleum Geologists Bulletin*, *57*, 349–369. https://doi.org/10.1306/819A4272-16C5-11D7-8645000102C1865D

Bernabé, Y., Li, M., & Maineult, A. (2010). Permeability and pore connectivity: A new model based on network simulations. *Journal of Geophysical Research*, *115*, 10203. https://doi.org/10.1029/2010JB007444

Bernabé, Y., Mok, U., & Evans, B. (2003). Permeability-porosity relationships in rocks subjected to various evolution processes. *Pure and Applied Geophysics*, *160*(5), 937–960. https://doi.org/10.1007/pl00012574

Bourbie, T., & Zinszner, B. (1985). Hydraulic and acoustic properties as a function of porosity in fontainebleau sandstone. *Journal of Geophysical Research*, *90*(B13), 11524. https://doi.org/10.1029/jb090ib13p11524

Clark, A. C., & Vanorio, T. (2016). The rock physics and geochemistry of carbonates exposed to reactive brines. *Journal of Geophysical Research: Solid Earth*, *121*, 1497–1513. https://doi.org/10.1002/2016JB013070

Clavaud, J.-B., Maineult, A., Zamora, M., Rasolofosaon, P., & Schlitter, C. (2008). Permeability anisotropy and its relations with porous medium structure. *Journal of Geophysical Research*, *113*(B1). https://doi.org/10.1029/2007jb005004

Clennell, M. B., Dewhurst, D. N., Brown, K. M., & Westbrook, G. K. (1999). Permeability anisotropy of consolidated clays. *Muds and Mudstones: Physical and Fluid-Flow Properties*, *158*, 79–96. https://doi.org/10.1144/GSL.SP.1999.158.01.07

Croize, D., Bjørlykke, K., Jahren, J., & Renard, F. (2010). Experimental mechanical and chemical compaction of carbonate sand. *Journal of Geophysical Research*, *115*, B11204. https://doi.org/10.1029/2010JB007697

Den Brok, B., Zahid, M., & Passchier, C. W. (1999). Pressure solution compaction of sodium chlorate and implications for pressure solution in NaCl. *Tectonophysics*, *307*(3–4), 297–312. https://doi.org/10.1016/s0040-1951(99)00103-1

Dewers, T., & Ortoleva, P. (1988). The role of geochemical self-organization in the migration and trapping of hydrocarbons. *Applied Geochemistry*, *3*(3), 287–316. https://doi.org/10.1016/0883-2927(88)90108-4

Doyen, P. M. (1988). Permeability, conductivity, and pore geometry of sandstone. *Journal of Geophysical Research*, *93*, 7729–7740. https://doi.org/10.1029/JB093iB07p07729

Ehrenberg, S. N. (2006). Porosity destruction in carbonate platforms. *Journal of Petroleum Geology*, *29*, 41–52. https://doi.org/10.1111/j.1747-5457.2006.00041.x

Faulkner, D. R., & Rutter, E. H. (1998). The gas permeability of clay-bearing fault gouge at 20 °C. *Geological Society of London, Special Publication*, *147*, 147–156. https://doi.org/10.1144/GSL.SP.1998.147.01.10

Fossen, H., Schultz, R. A., Shipton, Z. K., & Mair, K. (2007). Deformation bands in sandstone: A review. *Journal of the Geological Society of London*, *164*, 755–769. https://doi.org/10.1144/0016-76492006-036

Fusseis, F., Schrank, C., Liu, J., Karrech, A., Llana-Fúnez, S., Xiao, X., & Regenauer-Lieb, K. (2012). Pore formation during dehydration of a polycrystalline gypsum sample observed and quantified in a time-series synchrotron X-ray micro-tomography experiment. *Solid Earth*, *3*, 71–86. https://doi.org/10.5194/se-3-71-2012

Ghanbarzadeh, S., Hesse, M. A., Prodanović, M., & Gardner, J. E. (2015). Deformation-assisted fluid percolation in rock salt. *Science*, *350*, 1069–1072. https://doi.org/10.1126/science.aac8747

Gibson, R. G. (1998). Physical character and fluid-flow properties of sandstone-derived fault zones. *Geological Society of London, Special Publication*, *127*, 83–97.

Gratier, J. P. (1993). Experimental pressure solution of halite by an indenter technique. *Geophysical Research Letters*, *20*, 1647–1650.

Gratier, J. P., Dysthe, D. K., & Renard, F. (2013). The role of pressure solution creep in the ductility of the Earth's upper crust. *Advances in Geophysics*. https://doi.org/10.1016/B978-0-12-380940-7.00002-0

Greene, G. W., Kristiansen, K., Meyer, E. E., Boles, J. R., & Israelachvili, J. N. (2009). Role of electrochemical reactions in pressure solution. *Geochimica et Cosmochimica Acta*, *73*, 2862–2874. https://doi.org/10.1016/j.gca.2009.02.012

Gundersen, E., Renard, F., Dysthe, D. K., Bjørlykke, K., & Jamtveit, B. (2002). Coupling between pressure solution creep and diffusive mass transport in porous rocks. *Journal of Geophysical Research*, *107*(B11), 2317. https://doi.org/10.1029/2001jb000287

Head, D., & Vanorio, T. (2016). Effects of changes in rock microstructures on permeability: 3-D printing investigation. *Geophysical Research Letters*, *43*, 7494–7502. https://doi.org/10.1002/2016GL069334

Heap, M. J., Baud, P., Reuschle, T., & Meredith, P. G. (2014). Stylolites in limestones: Barriers to fluid flow? *Geology*, *42*, 51–54. https://doi.org/10.1130/G34900.1

Hiatt E. E., & Kyser K. (2000). Basin Analysis: Porosity and Permeability Evolution in Sedimentary Rocks. In *Fluids and Basin Evolution*. Mineralogical Association of Canada.

Hickman, S. H., & Evans, B. (1995). Kinetics of pressure solution at halite-silica interfaces and intergranular clay films. *Journal of Geophysical Research*, *100*, 13113–13132.

Ilgen, A. G., Heath, J. E., Akkutlu, I. Y., Bryndzia, L. T., Cole, D. R., Kharaka, Y. K., et al. (2017). Shales at all scales: Exploring coupled processes in mudrocks. *Earth-Science Reviews*, *166*, 132–152. https://doi.org/10.1016/j.earscirev.2016.12.013

Jamtveit, B., & Austrheim, H. (2010). Metamorphism: The role of fluids. *Elements*, *6*, 153–158. https://doi.org/10.2113/gselements.6.3.153

Jolivet, L., Raimbourg, H., Labrousse, L., Avigad, D., Leroy, Y., Austrheim, H., & Andersen, T. B. (2005). Softening trigerred by eclogitization, the first step toward exhumation during continental subduction. *Earth and Planetary Science Letters*, *237*, 532–547. https://doi.org/10.1016/j.epsl.2005.06.047

Jonas, L., John, T., King, H. E., Geisler, T., & Putnis, A. (2014). The role of grain boundaries and transient porosity in rocks as fluid pathways for reaction front propagation. *Earth and Planetary Science Letters*, *386*, 64–74. https://doi.org/10.1016/j.epsl.2013.10.050

Kampman, N., Bickle, M., Wigley, M., & Dubacq, B. (2014). Fluid flow and CO_2-fluid-mineral interactions during CO_2-storage in sedimentary basins. *Chemical Geology*, *369*, 22–50. https://doi.org/10.1016/j.chemgeo.2013.11.012

Keehm, Y. (2003). Computational rock physics: Transport properties in porous media and applications 135.

Keehm, Y., Mukerji, T., & Nur, A. (2001). Computational rock physics at the pore scale: Transport properties and diagenesis in realistic pore geometries. *The Leading Edge*, *20*. https://doi.org/10.1190/1.1438904

Krumbein, W. C., & Monk, G. D. (1943). Permeability as a function of the size parameters of unconsolidated sand. *Transactions of the AIME*, *151*(01), 153–163. https://doi.org/10.2118/943153-g

Loucks, R. G., Reed, R. M., Ruppel, S. C., & Hammes, U. (2012). Spectrum of pore types and networks in mudrocks and a descriptive classification for matrix-related mudrock pores. *AAPG Bulletin*, *96*(6), 1071–1098. https://doi.org/10.1306/08171111061

Macente, A., Fusseis, F., Butler, I. B., Tudisco, E., Hall, S. A., & Andò, E. (2018). 4D porosity evolution during pressure-solution of NaCl in the presence of phyllosilicates. *Earth and Planetary Science Letters*, *502*, 115–125. https://doi.org/10.1016/j.epsl.2018.08.032

Macente, A., Fusseis, F., Menegon, L., Xianghui, X., & John, T. (2017). The strain-dependent spatial evolution of garnet in a high-P ductile shear zone from the Western Gneiss Region (Norway): a synchrotron X-ray microtomography study. *Journal of Metamorphic Geology*, *35*. https://doi.org/10.1111/jmg.12245

Merino, E., Ortoleva, P., & Strickholm, P. (1983). Generation of evenly-spaced pressure-solution seams during late diagenesis. *Contributions to Mineralogy and Petrology*, *82*, 360–370.

Meyer, E. E., Greene, G. W., Alcantar, N. A., Israelachvili, J. N., & Boles, J. R. (2006). Experimental investigation of the dissolution of quartz by a muscovite mica surface: Implications for pressure solution. *Journal of Geophysical Research*, *111*, B08202. https://doi.org/10.1029/2005JB004010

Miller, K., Vanorio, T., & Keehm, Y. (2017). Evolution of permeability and microstructure of tight carbonates due to numerical simulation of calcite dissolution. *Journal of Geophysical Research: Solid Earth*, *122*, 4460–4474. https://doi.org/10.1002/2017JB013972

Mok, U., Bernabé, Y., & Evans, B. (2002). Permeability, porosity and pore geometry of chemically altered porous silica glass. *Journal of Geophysical Research*, *107*(B1), 2015. https://doi.org/10.1029/2001jb000247

Nelson, P. H. (1994). Permeability porosity relationships in sedimentary rocks. *Log Analyst*, 38–62.

Ngwenya, B. T., Kwon, O., Elphick, S. C., & Main, I. G. (2003). Permeability evolution during progressive development of deformation bands in porous sandstones. *Journal of Geophysical Research*, *108*(B7), 2343. https://doi.org/10.1029/2002JB001854

Noiriel, C., Bernard, D., Gouze, P., & Thibault, X. (2005). Hydraulic Properties and Microgeometry Evolution Accompanying Limestone Dissolution by Acidic Water. *Oil & Gas Science and Technology*, *60*(1), 177–192. https://doi.org/10.2516/ogst:2005011

Olsen, H. W. (1960). Hydraulic flow through saturated clays. *Clays and Clay Minerals*, *9*(1), 131–161. https://doi.org/10.1346/ccmn.1960.0090108

Ortoleva, P., Merino, E., Moore, C., & Chadam, J. (1987). Geochemical self-organization I; reaction-transport feedbacks and modeling approach. *American Journal of Science*, *287*(10), 979–1007. https://doi.org/10.2475/ajs.287.10.979

Pape, H., Clauser, C., & Iffland, J. (1999). Permeability prediction based on fractal pore-space geometry. *Geophysics*, *64*(5), 1447–1460. https://doi.org/10.1190/1.1444649

Pape, H., & Schopper, J. R. (1988). Relations between physically relevant geometrical properties of a multi-fractal porous system. *Studies in Surface Science and Catalysis*, 473–482. https://doi.org/10.1016/s0167-2991(09)60770-9

Pluymakers, A. M. H., & Spiers, C. J. (2015). Compaction creep of simulated anhydrite fault gouge by pressure solution: Theory v. experiments and implications for fault sealing. *Geological Society - Special Publications*, *409*, 107–124. https://doi.org/10.1144/SP409.6

Renard, F., Bernard, D., Thibault, X., & Boller, E. (2004). Synchrotron 3D microtomography of halite aggregates during experimental pressure solution creep and evolution of the permeability. *Geophysical Research Letters*, *31*, L07607. https://doi.org/10.1029/2004GL019605

Renard, F., Dysthe, D., Feder, J., Bjorlykke, K., & Jamtveit, B. (2001). Enchanced pressure solution creep rates induced by clay particles: Experimental evidence in salt aggregates. *Geophysical Research Letters*, *28*, 1295–1298. https://doi.org/10.1029/2000GL012394

Renard, F., Ortoleva, P., & Gratier, J. P. (1997). Pressure solution in sandstones: Influence of clays and dependence on temperature and stress. *Tectonophysics*, *280*, 257–266. https://doi.org/10.1016/S0040-1951(97)00039-5

Rotevatn, A., Fossmark, H. S., Bastesen, E., Thorsheim, E., & Torabi, A. (2016). Do deformation bands matter for flow? Insights from permeability measurements and flow simulations in porous carbonate rocks. *Petroleum Geoscience*, petgeo2016-038. https://doi.org/10.1144/petgeo2016-038

Rutter, E. H. (1983). Pressure solution in nature, theory and experiment. *Journal of the Geological Society of London*, *140*, 725–740. https://doi.org/10.1144/gsjgs.140.5.0725

Schutjens, P. M. T. M., & Spiers, C. J. (1999). Intergranular pressure solution in NaCl: Grain-to-grain contact experiments under the optical microscope. *Oil & Gas Science and Technology*, *54*, 729–750. https://doi.org/10.2516/ogst:1999062

Spiers, C. J., & Brzesowsky, R. H. (1993). Densification behaviour of wet granular salt: Theory versus experiment. *Seventh Symposium on Salt*, *1*, 83–92.

Spiers, C. J., Schutjens, P. M. T. M., Brzesowsky, R. H., Peach, C. J., Liezenberg, J. L., & Zwart, H. J. (1990). Experimental determination of constitutive parameters governing creep of rocksalt by pressure solution. *Geological Society of London, Special Publication*, *54*, 215–227. https://doi.org/10.1144/GSL.SP.1990.054.01.21

Sun, W., Andrade, J. E., Rudnicki, J. W., & Eichhubl, P. (2011). Connecting microstructural attributes and permeability from 3D tomographic images of in situ shear-enhanced compaction bands using multiscale computations. *Geophysical Research Letters*, *38*, L10302. https://doi.org/10.1029/2011GL047683

Urai, J. L., Spiers, C. J., Zwart, H. J., & Lister, G. S. (1986). Weakening of rock salt by water during long-term creep. *Nature*, *324*, 554–557. https://doi.org/10.1038/324554a0

van den Ende, M. P. A., Marketos, G., Niemeijer, A. R., & Spiers, C. J. (2018). Investigating compaction by intergranular pressure solution using the discrete element method. *Journal of Geophysical Research: Solid Earth*, *123*, 107–124. https://doi.org/10.1002/2017JB014440

Van der Land, C., Wood, R., Wu, K., van Dijke, M. I. J., Jiang, Z., Corbett, P. W. M., & Couples, G. (2013). Modelling the permeability evolution of carbonate rocks. *Marine and Petroleum Geology*, *48*, 1–7. https://doi.org/10.1016/j.marpetgeo.2013.07.006

Vanorio, T. (2015). Recent advances in time-lapse, laboratory rock physics for the characterization and monitoring of fluid-rock interactions. *Geophysics*, *80*, WA49–WA59. https://doi.org/10.1190/geo2014-0202.1

Weyl, P. K. (1959). Pressure solution and the force of crystallization: A phenomenological theory. *Journal of Geophysical Research*, *64*(11), 2001–2025. https://doi.org/10.1029/jz064i011p02001

Xing, X., Butler, D. L., & Yang, C. (2007). A lattice Boltzmann based single-phase method for modeling surface tension and wetting. *Computational Materials Science*, *39*(2), 282–290. https://doi.org/10.1016/j.commatsci.2006.06.007

Yardley, B. W. D. (2011). The role of water in the evolution of the continental crust. *Journal of the Geological Society*, *166*, 585–600. https://doi.org/10.1144/0016-76492008-101

Yoon, H., Kang, Q., & Valocchi, A. J. (2015). Lattice Boltzmann-based approaches for pore-scale reactive transport. *Reviews in Mineralogy and Geochemistry*, *80*, 393–431. https://doi.org/10.2138/rmg.2015.80.12

Zhang, X., & Spiers, C. J. (2005). Compaction of granular calcite by pressure solution at room temperature and effects of pore fluid chemistry. *International Journal of Rock Mechanics and Mining Sciences*, *42*, 950–960. https://doi.org/10.1016/j.ijrmms.2005.05.017

References From Supporting Information

Lindquist, W. B., Lee, S.-M., Coker, D. A., Jones, K. W., & Spanne, P. (1996). Medial axis analysis of void structure in three-dimensional tomographic images of porous media. *Journal of Geophysical Research*, *101*(B4), 8297–8310. https://doi.org/10.1029/95JB03039

Lorensen, W. E., & Cline, H. E. (1987). Marching cubes: A high resolution 3D surface construction algorithm. Proceedings of the 14th Annual Conference on Computer Graphics and Interactive Techniques - SIGGRAPH'87, 21(4), 163–169. https://doi.org/10.1145/37401.37422